

Structural and Stress Response of Nanotwinned $B_{13}CN$ under Large Strains

Hui Liang, Di Wang, Xianqi Song, Qing Guo,* and Quan Li*



Cite This: *J. Phys. Chem. Lett.* 2023, 14, 10475–10481



Read Online

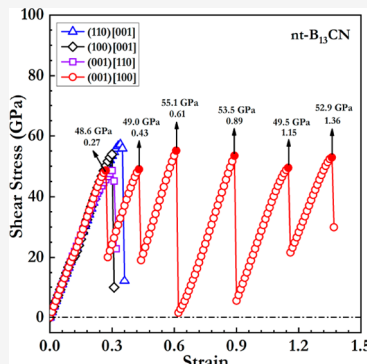
ACCESS |

Metrics & More

Article Recommendations

Supporting Information

ABSTRACT: Boron-rich carbides with icosahedral cages as pivotal structural units, which exhibit high hardness and low density, have promising industrial applications. However, the insufficient fracture toughness of these materials hinders their engineering applications. A recent first-principles study revealed that single-crystal $B_{13}CN$ (sc- $B_{13}CN$) exhibits interesting structural deformation modes and superior mechanical properties to boron-rich carbides, prompting us to further explore this intriguing material. Herein, we adopted sc- $B_{13}CN$ as an archetypal system owing to its excellent structural and mechanical properties to construct nanotwinned $B_{13}CN$ (nt- $B_{13}CN$) and explore its mechanical properties and structural deformation modes under large strains. We unraveled the specific stress-strain relationship of nt- $B_{13}CN$ and the considerable effect of twinning on its structural deformation modes under diverse loading conditions. Our results indicate that twinning leads to interesting structural deformation patterns and is extremely beneficial to improving the structural stability and mechanical properties of boron-rich materials. The current results provide an improved understanding of the theoretical design for various nanotwinned boron-rich materials with intricate bonding configurations.



Boron-rich carbides (e.g., B_4C and $B_{13}C_2$) are exemplary cases among boron-rich compounds that exhibit unique properties of high hardness (30–50 GPa) and low density ($\sim 2.5 \cdot g \cdot cm^{-3}$), with applications in body armor, cutting tools, and neutron radiation absorbents.^{1–10} However, owing to low fracture toughness (3–4 MPa·m^{1/2}),¹¹ B_4C exhibits brittle failure under high pressure while forming amorphous shear bands.^{12–16} To design and synthesize lightweight materials with excellent mechanical properties, various boron-rich compounds have been extensively explored, e.g., B_6O , $B_{13}C_2$, and $B_{13}CN$.^{17–23} In boron-rich compounds, a B_{12} icosahedron serves as the skeleton unit in which two-center two-electron (2c-2e) and three-center two-electron (3c-2e) bonding configurations coexist and exhibits unique bonding characteristics because of its electron-deficient nature.^{24–26} The mechanical properties of boron-rich compounds are highly sensitive to their electron-filling states because of the electron-deficient icosahedrons and electron-compensating atomic chains. Thus, understanding their mechanical properties under various electron-filling states is crucial. Recently, first-principles calculations showed that the B_{12} icosahedron exhibits enhanced stability via N-induced electron compensation, and this highly stable unit endows superior structural stability and mechanical strengths to the boron-rich compound $B_{13}CN$.²³

To improve the mechanical properties of $B_{13}CN$, we adopted the structural twinning method, which remarkably stiffens diamond and c -BN, resulting in considerable strength enhancement and unprecedented Vickers hardness values of

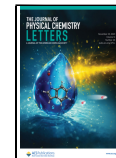
200 and 108 GPa, respectively.^{27–30} For nanotwinned diamond and nanotwinned c -BN, this enhanced hardness can be attributed to the twin boundaries (TBs) present in the structure which promote a stress concentration in the unit cell, leading to a bond rearrangements mechanism that produces a significant indentation strain stiffening by inhibiting the graphitization process or bond collapse failure mode.^{28,30} These TBs effectively change the structural deformation modes of the material under large strains, and the material thus exhibits mechanical behavior that is different from the mechanical behavior of a single-crystal structure. Another hardness enhancement mechanism that is completely different from diamond is the defect (twinning)-induced structural stabilizing mechanism in B_4C , which reduces energy by releasing the native strains built in the single crystal, forming a highly nanotwinned structure that is more stable than the single-crystal structure.⁷ The structural twinning approach has mainly been applied to study the structural and mechanical properties of metals and strong covalent solids with simple structures that exhibit improved and more versatile mechanical characteristics.^{31–37} A pressing task is to explore fascinating

Received: October 16, 2023

Revised: November 10, 2023

Accepted: November 13, 2023

Published: November 15, 2023



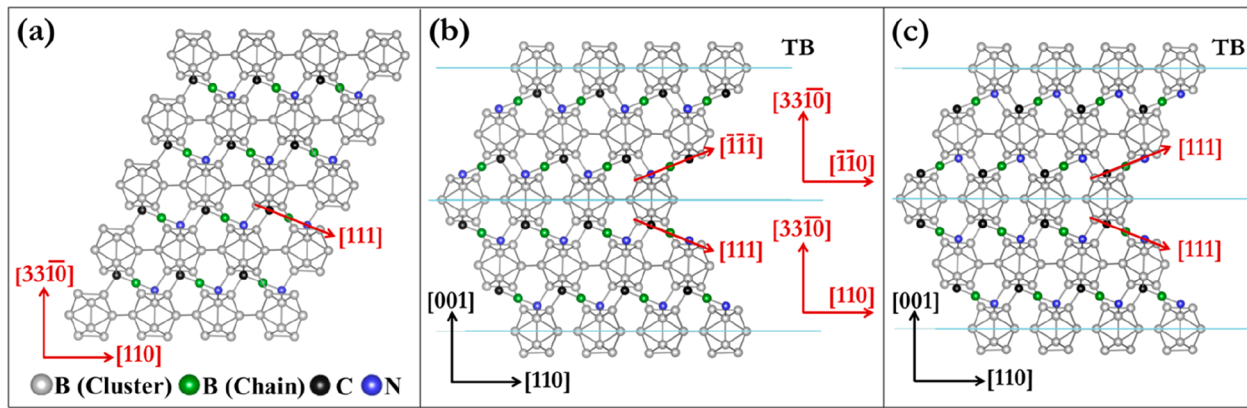


Figure 1. Structural models of $B_{13}CN$. (a) Structure of sc- $B_{13}CN$ based on the $(3\bar{3}\bar{1}0)[110]$ slip system. (b) Structure of asymmetric nt- $B_{13}CN$, where the TB is along the (001) plane. (c) Structure of symmetric nt- $B_{13}CN$, where the TB is along the (001) plane. The direction from C to N atoms in the triatomic chains of sc- $B_{13}CN$ (rhombohedral structure) is defined as $[111]$, and the vice versa is defined as $[\bar{1}\bar{1}\bar{1}]$; “TB” is represented by a solid line, and the direction of the triatomic chain is represented by an arrow.

nanotwinned structures in various covalent solids with complex bond structures, which may lead to the optimization of mechanical properties and fundamental understanding of the underlying physics.^{38–42} Herein, we selected single-crystal $B_{13}CN$ (sc- $B_{13}CN$) with improved structural stability and mechanical properties as a structural prototype to construct nanotwinned $B_{13}CN$ (nt- $B_{13}CN$). We subsequently analyzed the mechanical properties and structural deformation modes of nt- $B_{13}CN$ under large strains.

We constructed nt- $B_{13}CN$ using a nanotwinned model with 60 atoms to reveal the effect of twinning on its structural deformation modes under large strains and compared the results with those of sc- $B_{13}CN$. First-principles calculations show that nt- $B_{13}CN$ exhibits repetitive stress responses under large shear strains, and its ideal strength is higher than that of sc- $B_{13}CN$ under tensile strains. Notably, twinning has a more specific effect on the mechanical properties and associated structural deformation modes of nt- $B_{13}CN$ under shear loading strains; that is, the icosahedrons in nt- $B_{13}CN$ can retain their integrity over the entire shear deformation range, enabling that the structure can resist further deformation, and this behavior is different from that of sc- $B_{13}CN$. These results indicate that twinning can result in intriguing structural deformation patterns, which may be effective for enhancing the structural and mechanical properties of other boron-rich compounds.

Based on the structural arrangement of sc- $B_{13}CN$, symmetric and asymmetric nt- $B_{13}CN$ were reasonably designed (Figure 1). Although the basic structural units comprise icosahedral cages and triatomic chains, the two twins of $B_{13}CN$ are considerably different from the symmetric and asymmetric twins observed for B_4C because of the difference between the basic structural units of the two single-crystal structures. B_4C contains $B_{11}C$ clusters and triatomic C–B–N chains, while $B_{13}CN$ comprises B_{12} icosahedra and triatomic C–B–N chains. Therefore, the structural diversity of B_4C stems from the different relative arrangements of the C atoms in the $B_{11}C$ icosahedron, while that of $B_{13}CN$ can be ascribed to the different relative positions of the three atoms in the C–B–N triatomic chain. The structures of sc- $B_{13}CN$, asymmetric nt- $B_{13}CN$, and symmetric nt- $B_{13}CN$ are shown in Figure 1(a)–(c), respectively. Sc- $B_{13}CN$ can be described as a boron-rich rhombohedral phase with $R\bar{3}m$ symmetry; each unit cell contains 15 atoms with icosahedral B_{12} clusters and triatomic

C–B–N chains. We constructed a bilayer nanotwinned structure, comprising two icosahedral layers and two triatomic chain layers, and in this structure, the TB was along the (001) plane with a separation of $\lambda = 0.906$ nm. Our calculations aim to investigate the intrinsic influence of twinning on the stress response behavior and the corresponding structural deformation pattern of $B_{13}CN$ under large strains. The orientations of the triatomic C–B–N chains on either side of the TB are different in asymmetric and symmetric nt- $B_{13}CN$. In asymmetric nt- $B_{13}CN$, the triatomic chain on one side of the TBs is oriented along the $[111]$ direction, and that on the other side is oriented along the $[\bar{1}\bar{1}\bar{1}]$ direction [Figure 1(b)]. In symmetric nt- $B_{13}CN$, the triatomic chains on both sides of the TBs are oriented along the $[111]$ direction, as shown in Figure 1(c).

To determine the structural stability of nt- $B_{13}CN$, we quantitatively evaluated and compared its energy with that of sc- $B_{13}CN$. Our results show that the energy of asymmetric nt- $B_{13}CN$ is (1.9 meV/atom) lower than that of symmetric nt- $B_{13}CN$, and even (0.3 meV/atom) lower than that of sc- $B_{13}CN$, indicating that asymmetric nt- $B_{13}CN$ exhibits superior thermodynamic stability. Therefore, asymmetric nt- $B_{13}CN$ is selected as an exemplary case to demonstrate fundamental structural and mechanical properties at large strains. Phonon spectrum calculations and ab initio molecular dynamics (AIMD) simulations of nt- $B_{13}CN$ were performed to verify its structural stability. The phonon dispersion curves show that imaginary frequencies are absent in the whole Brillouin zone, confirming the dynamic stability of nt- $B_{13}CN$ [Figure 2(a)]. The calculated mean-squared displacements of the atomic positions at different times show that the system reaches equilibrium at 300 K and is thermodynamically stable [Figure 2(b)].

To investigate the bonding characteristics of nt- $B_{13}CN$, we calculated the projected density of states (PDOS). The results show that nt- $B_{13}CN$ is a semiconductor with a bandgap of 2.4 eV [Figure 3(a)], which is close to that of sc- $B_{13}CN$ (2.7 eV),²³ indicating that twinning has no substantial effect on the electronic properties of $B_{13}CN$. Moreover, the DOS results show that the 2p state of boron is dominantly occupied. Thus, the structural deformation resistance of nt- $B_{13}CN$ can be attributed to the B–B covalent bonds present in the B_{12} icosahedron, i.e., the skeleton unit. We also calculated the

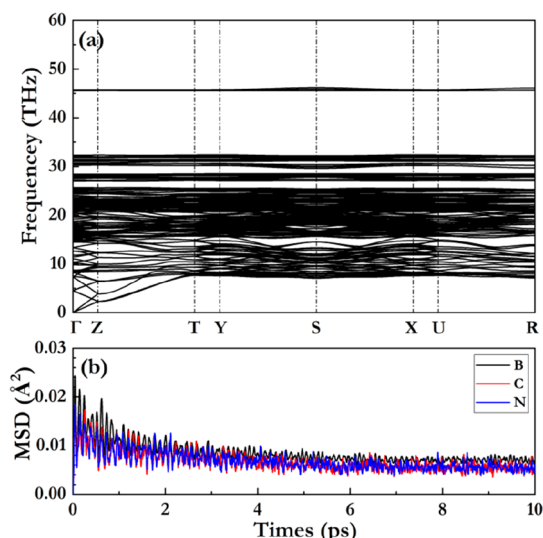


Figure 2. (a) Phonon dispersion of nt-B₁₃CN. (b) Mean-squared displacements of atomic positions versus time of nt-B₁₃CN at 300 K.

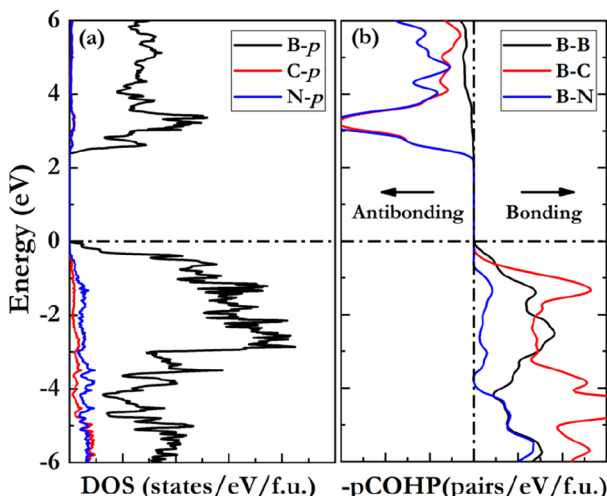


Figure 3. (a) PDOS of the B-p, C-p, and N-p orbitals in nt-B₁₃CN. (b) Projected crystal orbital Hamiltonian population (-pCOHP) of nt-B₁₃CN.

projected crystal orbital Hamiltonian population (pCOHP) of nt-B₁₃CN, which assesses the weighted wave function population of the two atomic orbitals of the selected B-B, B-C, and B-N pairs, and the corresponding results are shown in Figure 3(b). In nt-B₁₃CN, no antibonding state is occupied below the Fermi level, indicating that the structure is highly stable. Notably, the proportion of B-B antibonding states above the Fermi level is small, indicating a strong B-B bonding in nt-B₁₃CN; this result can be attributed to the B₁₂ icosahedron skeleton of the structure. We also used the CASTEP code⁴³ to examine the Mulliken populations of the covalent bonds in nt-B₁₃CN and sc-B₁₃CN. Evidently, the average Mulliken population of the covalent bonds in nt-B₁₃CN is 0.616, which is comparable with that of the bonds present in sc-B₁₃CN (0.625). These similar Mulliken populations indicate that the nanotwinning in nt-B₁₃CN does not affect the strength of the covalent bonds, which determines the mechanical properties of the material at equilibrium.

To assess the mechanical properties of nt-B₁₃CN under small loading conditions, we evaluated the elastic parameters by introducing small strains near the equilibrium structures. The resulting C_{ij} values satisfy the mechanical stability criteria, verifying the mechanical stability of nt-B₁₃CN. The bulk modulus B (250.2 GPa), shear modulus G (198.3 GPa), and Young's modulus E (470.6 GPa) of nt-B₁₃CN were extracted from the elastic constants, and the values were almost identical to those of sc-B₁₃CN.²³ We also evaluated the hardness values of sc-B₁₃CN and nt-B₁₃CN using a well-developed semi-empirical model,^{44–46} and the resulting simulated Vickers hardness of sc-B₁₃CN was found to be 30.6 GPa. Considering the contribution of the Hall-Petch effect (H_{HP})^{47,48} and quantum confinement effect (H_{qc})⁴⁹ to the hardness, nt-B₁₃CN exhibits a hardness of 48.7 GPa at a size of 50 nm.

Subsequently, we evaluated the mechanical response of nt-B₁₃CN to large strains to probe the effect of twinning on its fundamental structural and mechanical properties. We first investigated the tensile stress-strain relationship of nt-B₁₃CN and determined the easy-cleavage plane by calculating its tensile strength along various high-symmetry directions. Results show that the lowest peak tensile stress (i.e., the ideal tensile strength) of nt-B₁₃CN is 52.9 GPa along the [001] direction [Figure 4(a)].

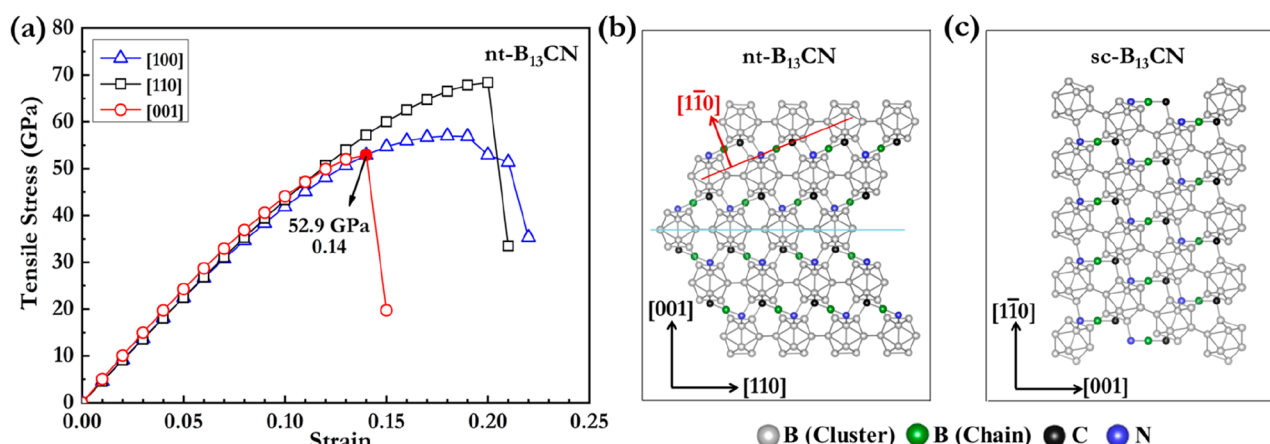


Figure 4. (a) Stress-strain relationship curves of nt-B₁₃CN under different tensile strains. The data were obtained via first-principles calculations along the indicated crystallographic directions. The solid circle indicates the ideal tensile strength, and the corresponding data point is obtained at a strain of 0.14. (b) Structure of nt-B₁₃CN along the easy [001] tensile direction. The red arrow indicates the easy tensile direction of sc-B₁₃CN. (c) Structure of sc-B₁₃CN along with the easy [110] tensile direction.

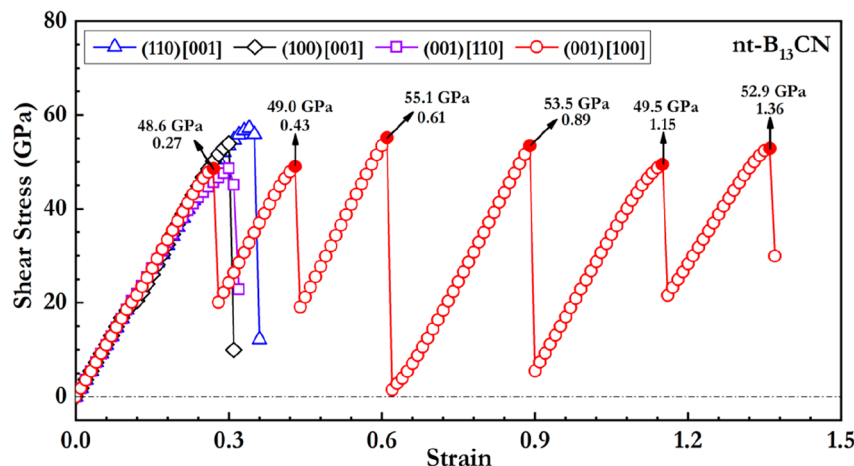


Figure 5. Calculated stress–strain relationship curves of nt-B₁₃CN along the directions parallel and perpendicular to the TB under pure shear deformation. The solid circles indicate atomic structure deformation before structural glide.

To understand the distinct effect of TBs on the mechanical response of nt-B₁₃CN under tensile deformation, we compared the stress response of nt-B₁₃CN with that of sc-B₁₃CN, which was reported in a recent study.²³ The ideal tensile strength of sc-B₁₃CN is 51.2 GPa along the [1̄10] direction, which is perpendicular to the direction of the triatomic chain in the structure.²³ By contrast, the ideal tensile strength of nt-B₁₃CN is ~3.3% higher than that of sc-B₁₃CN, primarily because of the twinning-induced diversification of the triatomic chain orientations in the nt-B₁₃CN structure and the absence of a crystal plane being perpendicular to that of the triatomic chains in the structure. Thus, the easy tensile direction of sc-B₁₃CN is eliminated through twinning, resulting in a considerably increased ideal tensile strength of B₁₃CN (52.9 GPa). The weakest tensile directions of nt-B₁₃CN and sc-B₁₃CN (i.e., the [001] and [1̄10] directions) are marked in Figure 4(b), while the [1̄10] direction of sc-B₁₃CN is also displayed in Figure 4(c). The relevant structural snapshots of nt-B₁₃CN deformed along the easy tensile [001] direction are shown in Supporting Information Figure S1.⁵⁰ The increased ideal tensile strength of nt-B₁₃CN implies that the presence of TBs is beneficial for tuning the mechanical response of these materials.

Subsequently, we evaluated the structural and stress responses of nt-B₁₃CN under shear deformation, and the corresponding stress–strain curves are presented in Figure 5. The calculated tensile stress–strain curves of nt-B₁₃CN (as shown in Figure 4) indicate that the weakest stress response, observed in the [001] direction, results in a (001) easy-cleavage plane. To obtain a more comprehensive understanding of the ultimate mechanical strength and intrinsic structural response of nt-B₁₃CN under shear strains, two other feasible cleavage planes, namely, (100) and (110), were also considered. Among the four shear slip systems discussed thus far, two systems are parallel to the TB plane, while the remaining two systems are perpendicular to the TB plane. Here, we mainly focus on the (001)[100] and (001)[110] directions, which are parallel to the TB plane and exhibit low shear strengths.

In the (001)[100] shear direction, nt-B₁₃CN exhibits a special stress response; i.e., the stress repeats with the increasing strain, and the toughness improves. This interesting phenomenon can be attributed to the effect of twinning on the structural deformation modes of B₁₃CN. Because of the

existence of TBs in the nt-B₁₃CN structure, the deformation modes of nt-B₁₃CN are different from those of sc-B₁₃CN throughout the deformation process (see Figure S2 for details).⁵⁰ Specifically, the triatomic chains along four non-equivalent glide planes of nt-B₁₃CN sequentially fracture over a large strain range, thereby releasing the stress at each fracture, ensuring the integrity of the icosahedron, and maintaining the stability of B₁₃CN. Finally, nt-B₁₃CN exhibits a stress repetition phenomenon throughout the strain range, and because of such unique deformation modes, nt-B₁₃CN exhibits continuous shearing in a large strain range until all the triatomic chains in the structure fracture. Eventually, nt-B₁₃CN degenerates into new sc-B₁₃CN.

We note another unusual phenomenon that the (001)[110] direction, also parallel to the TB plane, does not exhibit stress repetition similar to that of the (001)[100] direction. To understand this inconsistent phenomenon, we performed a close analysis of the structural changes in the (001)[110] direction under a strain and compared the results with those for the (001)[100] direction (see Figure S3 for details).⁵⁰ Evidently, the structural deformation mode that results in stress repetition along the (001)[100] shear slip direction of nt-B₁₃CN originates from the fracture of the triatomic chains before the collapse of the icosahedrons. By contrast, the structural deformation mode along the (001)[110] shear slip direction corresponds to the preferential fracture of the icosahedrons over the triatomic chains, and thus, no stress repetition is observed. These results reveal that in nt-B₁₃CN, if the triatomic chains fracture first, while the icosahedrons remain intact, then the structure continues shearing; otherwise, the icosahedrons fracture and then the structure directly collapses. Further analysis shows that under shear deformation, the stress on the triatomic chains in nt-B₁₃CN can be decomposed into tangential and radial stress components. When the tangential stress is dominant under the shear deformation, the triatomic chains in nt-B₁₃CN rupture first to release the stress in the system effectively, thereby further stabilizing the icosahedrons and allowing structural shearing. Therefore, the system shows a macroscopic stress repetition behavior in the (001)[100] direction. When the radial stress is dominant under the shear deformation, the icosahedrons are destroyed first, and the structure directly collapses without exhibiting stress repetition (for example, the results observed

for a shear process in the (001)[110] direction). Such contrasting deformation behaviors indicate that effectively avoiding or delaying the destruction of the icosahedrons in nt-B₁₃CN is essential for improving the mechanical properties of boron-rich compounds.

The mechanical behavior of sc-B₁₃CN under shear strains was comparatively examined (as shown in Figure 6) to probe

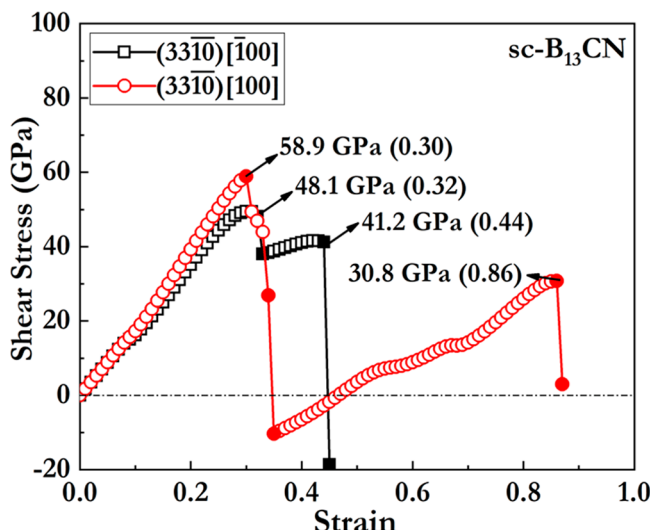


Figure 6. Stress–strain relationship curves of sc-B₁₃CN, obtained under shear deformation. The solid circles/squares indicate considerable deformation of sc-B₁₃CN at key strains.

the repetitive stress response and enhanced toughness of nt-B₁₃CN under large shear deformation. We define the (33̄10) crystallographic plane of sc-B₁₃CN as the (001) crystallographic plane of nt-B₁₃CN and perform calculations in the (33̄10)[100] and (331̄0)[100] crystallographic directions of sc-B₁₃CN under shear strains; these directions correspond to the (001)[100] crystallographic direction with a repeated stress response in nt-B₁₃CN [Figure 1(b)]. Sc-B₁₃CN exhibits a stepped stress response along the (33̄10)[100] shear direction, and the detailed structural deformation over the entire strain range is shown in Figure S4(a). The most important phenomena in the first stress release process include rotation and elongation of the triatomic chains and slight deformation of the icosahedrons. During the second stress release process, sc-B₁₃CN exhibits icosahedral disintegration and triatomic chain destruction, resulting in its structural collapse. Sc-B₁₃CN shows a two-stage shear deformation behavior along the (331̄0)[100] shear direction, and this behavior is different from that observed in the (33̄10)[100] direction [see Figure S4(b) for details].⁵⁰ The strain energy released at a strain of 0.35 considerably decreases the stress, completing the first stage of shear deformation (Figure 6). The fracture of all of the triatomic chains (strain = 0.35) in sc-B₁₃CN results in the recovery of the icosahedrons, and the C and N atoms in the triatomic chains form covalent bonds [Figure S4(b)]. Further shearing leads to the second-stage deformation. Under a shear stress, the C and N atoms in the triatomic chains form covalent bonds. Consequently, the triatomic chains lose their original flexibility and cannot release the stress in the system via rotation to maintain the integrity of the icosahedrons and stability of the structure. Therefore, premature deformation of the icosahedrons causes mechanical instability in sc-B₁₃CN. At

a strain of 0.87, the structure collapses with the disintegration of the icosahedrons. Therefore, sc-B₁₃CN does not show stress repetition, like nt-B₁₃CN with TBs, under a shear strain. Such a stress repetition phenomenon induced by twin boundaries in nt-B₁₃CN may be effective for structural and mechanical enhancement of other boron-rich compounds and offer insights into a broader variety of covalent crystals with intricate bonding networks.

A comprehensive first-principles calculation was performed to evaluate the stress–strain relationships of nt-B₁₃CN under shear loading conditions. Further, we systematically compared the mechanical responses of nt-B₁₃CN and sc-B₁₃CN to assess the effect of twinning on the intrinsic structural and stress responses of B₁₃CN. Results indicate that sc-B₁₃CN does not show any stress repetition behavior, suggesting that twinning has a profound effect on the deformation mode of the structure. Our results further reveal an intriguing shear strain-induced stress repetition phenomenon in nt-B₁₃CN, resulting from the special deformation modes of nt-B₁₃CN. In these deformation modes, the triatomic chain layers sequentially fracture to release the stresses accumulated over a large strain range, thus ensuring that the icosahedron remains stable throughout the shear deformation range. Upon further deformation, the triatomic chains fracture, and the icosahedrons disintegrate, resulting in structural collapse. Twinning leads to rich orientation of triatomic chains in nt-B₁₃CN, exhibiting a high resistance to structural deformation as well as rich structural characteristics under an applied strain, resulting in stress repetition. In addition, the TBs affect only the stress response pattern of nt-B₁₃CN under large strains; they do not influence the electronic properties of this material. The present results highlight the significance of twinning, which can lead to interesting structural deformation modes that can effectively improve the structural stability and mechanical properties of materials. The current calculation results provide fundamental insights into the design of other nanotwinned boron-rich materials with intricate bonding structures.

COMPUTATIONAL METHODS

Density functional theory calculations, including first-principles energetic calculations and ideal strength calculations, were performed using the VASP code⁵¹ with the projector augmented wave pseudopotentials.⁵² Further, the local density approximation⁵³ was used to describe the exchange-correlation potential. A 520 eV energy cutoff and Monkhorst–Pack⁵⁴ grid with a spacing of 0.2 Å⁻¹ were used for the subsequent computational process to ensure that the energy, stress, and force were within 1 meV per atom, 0.1 GPa, and 0.001 eV·Å⁻¹, respectively. Ab initio molecular dynamics (AIMD) simulations of the NVT ensemble were performed in 540 atomic units at 300 K. Phonon calculations were performed using the supercell method⁵⁵ and forces derived using the Hellmann–Feynman theorem.⁵⁶ The elastic constants were calculated using the stress–strain method, and the elastic moduli were then derived using the Voigt–Reuss–Hill averaging scheme. The chemical bonding properties were quantitatively described with the Crystal orbital Hamilton populations (COHPs)⁵⁷ as implemented in the LOBSTER program.⁵⁸ The quasistatic ideal strength and relaxed loading path were determined using the established stress–strain method^{59–65} in which the lattice vectors were incrementally deformed along the direction of the applied (tensile or shear) strains. At each step, the applied (tensile or shear) strain was fixed to determine the tensile or

shear stress, while the other five independent components of the strain tensors as well as all the atoms inside the unit cell were simultaneously relaxed until (i) all the residual components of the Hellmann–Feynman stress tensor that were orthogonal to the applied strain were <0.1 GPa and (ii) the force on each atom became negligible. The shape of the (deformed) unit cell and atomic relaxation were determined via constrained structural optimization at each step.

■ ASSOCIATED CONTENT

SI Supporting Information

The Supporting Information is available free of charge at <https://pubs.acs.org/doi/10.1021/acs.jpcllett.3c02890>.

Detailed fracture patterns of the nt-B₁₃CN and sc-B₁₃CN under different strains ([PDF](#))

■ AUTHOR INFORMATION

Corresponding Authors

Qing Guo — State Key Lab of Superhard Materials and Key Laboratory of Material Simulation Methods & Software of Ministry of Education, College of Physics, Jilin University, Changchun 130012, China; Email: qingguo@jlu.edu.cn

Quan Li — State Key Lab of Superhard Materials and Key Laboratory of Material Simulation Methods & Software of Ministry of Education, College of Physics and International Center of Future Science, Jilin University, Changchun 130012, China; [orcid.org/0000-0002-7724-1289](#); Email: liquan77@jlu.edu.cn

Authors

Hui Liang — State Key Lab of Superhard Materials and Key Laboratory of Material Simulation Methods & Software of Ministry of Education, College of Physics, Jilin University, Changchun 130012, China

Di Wang — State Key Lab of Superhard Materials and Key Laboratory of Material Simulation Methods & Software of Ministry of Education, College of Physics and International Center of Future Science, Jilin University, Changchun 130012, China

Xianqi Song — State Key Lab of Superhard Materials and Key Laboratory of Material Simulation Methods & Software of Ministry of Education, College of Physics and International Center of Future Science, Jilin University, Changchun 130012, China; [orcid.org/0000-0002-4758-5865](#)

Complete contact information is available at:

<https://pubs.acs.org/10.1021/acs.jpcllett.3c02890>

Notes

The authors declare no competing financial interest.

■ ACKNOWLEDGMENTS

This research is supported by the National Key Research and Development Program of China (Grant Nos. 2018YFA0703404 and 2021YFA1400503), Natural Science Foundation of China (Grant Nos. T2325013, 12074140, 52288102, 52090024, and 12034009), China Postdoctoral Science Foundation (Grant No. 2023M731296), and Program for Jilin University (JLU) Science and Technology Innovative Research Team. Reported calculations utilized computing facilities at the High-Performance Computing Center of Jilin University.

■ REFERENCES

- (1) Thevenot, F. Boron Carbide-A Comprehensive Review. *J. Eur. Ceram. Soc.* **1990**, *6*, 205–225.
- (2) Nelmes, R. J.; Loveday, J. S.; Wilson, R. M.; Marshall, W. G.; et al. Observation of Inverted-Molecular Compression in Boron Carbide. *Phys. Rev. Lett.* **1995**, *74*, 2268.
- (3) Emin, D. Unusual Properties of Icosahedral Boron-Rich Solids. *J. Solid State Chem.* **2006**, *179*, 2791–2798.
- (4) Chen, M. W.; McCauley, J. W.; Hemker, K. J. Shock-Induced Localized Amorphization in Boron Carbide. *Science* **2003**, *299*, 1563–1566.
- (5) Shirai, K. Electronic structures and mechanical properties of boron and boron-rich crystals (Part I). *J. Superhard Mater.* **2010**, *32*, 205–225.
- (6) Domnich, V.; Reynaud, S.; Haber, R. A.; Chhowalla, M. Boron Carbide: Structure, Properties, and Stability Under Stress. *J. Am. Ceram. Soc.* **2011**, *94*, 3605–3628.
- (7) Song, X.; Liu, C.; Li, Q.; Ma, Y.; Chen, C. Intrinsic dense twinning via release of native strain. *Acta. Mater.* **2023**, *257*, No. 119151.
- (8) Li, J.; An, Q.; Liu, L. S. Local amorphization in boron carbide at finite temperature: Strategies toward improved ductility. *Phys. Rev. B* **2021**, *104*, No. 134105.
- (9) He, Y.; Shen, Y. D.; Tang, B.; An, Q. Illuminating the photomechanical effect: Exploring the relationship between electron-hole excitation and deformation mechanisms in nanotwinned boron carbide. *Phys. Rev. B* **2023**, *107*, No. 224102.
- (10) Li, J.; An, Q. Nanotwinning-induced pseudoplastic deformation in boron carbide under low temperature. *Int. J. Mech. Sci.* **2023**, *242*, No. 107998.
- (11) Solozhenko, V. L.; Kurakevych, O. O.; Andrault, D.; Le Godec, Y.; Mezouar, M. Ultimate Metastable Solubility of Boron in Diamond: Synthesis of Superhard Diamond-like BC₅. *Phys. Rev. Lett.* **2009**, *102*, No. 015506.
- (12) Grady, D. E. Shock-Wave Compression of Brittle Solids. *Mech. Mater.* **1998**, *29*, 181–203.
- (13) Yan, X. Q.; Tang, Z.; Zhang, L.; Guo, J. J.; Jin, C. Q.; Zhang, Y.; Goto, T.; McCauley, J. W.; Chen, M. W. Depressurization Amorphization of Single-Crystal Boron Carbide. *Phys. Rev. Lett.* **2009**, *102*, 75505.
- (14) Reddy, K. M.; Liu, P.; Hirata, A.; Fujita, T.; Chen, M. W. Atomic Structure of Amorphous Shear Bands in Boron Carbide. *Nat. Commun.* **2013**, *4*, 2483.
- (15) An, Q.; Goddard, W. A.; Cheng, T. Atomistic Explanation of Shear-induced Amorphous Band Formation in Boron Carbide. *Phys. Rev. Lett.* **2014**, *113*, No. 095501.
- (16) Xie, K. Y.; An, Q.; Toksoy, M. F.; McCauley, J. W.; Haber, R. A.; Goddard, W. A.; Hemker, K. J. Atomic-Level Understanding of “Asymmetric Twins” in Boron Carbide. *Phys. Rev. Lett.* **2015**, *115*, No. 175501.
- (17) He, D.; Zhao, Y.; Daemen, L.; Qian, J.; Shen, T. D.; Zerda, T. W. Boron Suboxide: As Hard As Cubic Boron Nitride. *Appl. Phys. Lett.* **2002**, *81*, 643.
- (18) Guo, X.; He, J.; Liu, Z.; Tian, Y.; Sun, J.; Wang, H. T. Bond Ionicities and Hardness of B₁₃C₂-like Structured ByX Crystals (X = C, N, O, P, As). *Phys. Rev. B* **2006**, *73*, No. 104115.
- (19) An, Q.; Goddard, W. A. Nanotwins Soften Boron-Rich Boron Carbide (B₁₃C₂). *Appl. Phys. Lett.* **2017**, *110*, No. 111902.
- (20) Wang, L.; Wei, X.; Hao, X.; Song, X.; Yang, G.; Lu, C.; Chen, Y.; Wang, L.; Gao, G.; Tian, Y. Novel Boron-rich Phosphides with High Hardness, Large Strain, and Magnetism. *J. Phys. Chem. Lett.* **2023**, *14*, 1310–1317.
- (21) Kilic, M. E.; Jena, P. Catalytic Potential of [B₁₂X₁₁]²⁻ (X = F, Cl, Br, I, CN) Dianions. *J. Phys. Chem. Lett.* **2023**, *14*, 8697–8701.
- (22) Wang, L.; Sun, R.; Liu, W.; Yuan, Z.; Bergara, A.; Liang, X.; Chen, S.; Zhou, X. F.; Xu, B.; He, J.; Yu, D.; et al. Novel Superhard Boron-Rich Nitrides Under Pressure. *Sci. China. Mater.* **2020**, *63*, 2358–2364.

- (23) Liang, H.; Li, Q.; Chen, C. Atomistic Mechanisms for Contrasting Stress-Strain Relations of $B_{13}CN$ and $B_{13}C_2$. *J. Phys. Chem. Lett.* **2020**, *11*, 10454–10462.
- (24) He, J.; Wu, E.; Wang, H.; Liu, R.; Tian, Y. Ionicities of Boron-Boron Bonds in B_{12} Icosahedra. *Phys. Rev. Lett.* **2005**, *94*, No. 015504.
- (25) Oganov, A. R.; Chen, J.; Gatti, C.; Ma, Y.; Ma, Y.; Glass, C. W.; Liu, Z.; Yu, T.; Kurakevych, O. O.; Solozhenko, V. L. Ionic High-Pressure Form of Elemental Boron. *Nature* **2009**, *457*, 863–867.
- (26) Zhou, W.; Sun, H.; Chen, C. Soft Bond-Deformation Paths in Superhard-Boron. *Phys. Rev. Lett.* **2010**, *105*, No. 215503.
- (27) Tian, Y.; Xu, B.; Yu, D.; Ma, Y.; Wang, Y.; Jiang, Y.; Hu, W.; Tang, C.; Gao, Y.; Luo, K.; Zhao, Z.; et al. Ultrahard Nanotwinned Cubic Boron Nitride. *Nature (London)* **2013**, *493*, 385–388.
- (28) Li, B.; Sun, H.; Chen, C. Large Indentation Strain Stiffening in Nanotwinned Cubic Boron Nitride. *Nat. Commun.* **2014**, *5*, 4965.
- (29) Huang, Q.; Yu, D.; Xu, B.; Hu, W.; Ma, Y.; Wang, Y.; Zhao, Z.; Wen, B.; He, J.; Liu, Z.; Tian, Y. Nanotwinned Diamond with Unprecedented Hardness and Stability. *Nature (London)* **2014**, *510*, 250–253.
- (30) Li, B.; Sun, H.; Chen, C. Extreme Mechanics of Probing the Ultimate Strength of Nanotwinned Diamond. *Phys. Rev. Lett.* **2016**, *117*, No. 116103.
- (31) Pan, Q. S.; Lu, L. Strain-controlled cyclic stability and properties of Cu with highly oriented nanoscale twins. *Acta Mater.* **2014**, *81*, 248–257.
- (32) Wang, M.; Xu, X. Y.; Wang, H. Y.; He, L. H.; Huang, M. X. Evolution of dislocation and twin densities in a Mg alloy at quasi-static and high strain rates. *Acta Mater.* **2020**, *201*, 102–113.
- (33) Sun, Y. A.; Luo, Z. P.; Li, X. Y.; Lu, K. Effects of stacking fault energy on deformation induced grain boundary relaxation in nanograined Cu alloys. *Acta Mater.* **2022**, *239*, No. 118256.
- (34) Zhao, H. Z.; You, Z. S.; Tao, N. R.; Lu, L. Anisotropic toughening of nanotwin bundles in the heterogeneous nanostructured Cu. *Acta Mater.* **2022**, *228*, No. 117748.
- (35) Duan, F.; Li, Q.; Shen, Z.; Jiang, Z.; Liu, W.; Yan, Y.; Pan, J.; Sun, L.; Lu, J. Anisotropic mechanical properties and deformation mechanisms of nanotwinned Ni and Ni alloys with extremely fine twin boundary spacings. *Acta Mater.* **2023**, *260*, No. 119311.
- (36) Min, N.; Liang, H.; Chen, H.; Song, X.; Zhou, D.; Li, Q. Theoretical design of superhard twinned BC_2N . *Scr. Mater.* **2024**, *240*, No. 115843.
- (37) Han, Z.; Liu, H.; Li, Q.; Zhou, D.; Lv, J. Superior Mechanical Properties of GaAs driven by lattice nanotwinning. *Chin. Phys. Lett.* **2021**, *38*, No. 046201.
- (38) Lu, K. Stabilizing nanostructures in metals using grain and twin boundary architectures. *Nat. Rev. Mater.* **2016**, *1*, 1–13.
- (39) Yue, Y.; Gao, Y.; Hu, W.; Xu, B.; Wang, J.; Zhang, X.; Zhang, Q.; Wang, Y.; Ge, B.; Yang, Z.; Li, Z.; et al. Hierarchically Structured Diamond Composite with Exceptional Toughness. *Nature (London)* **2020**, *582*, 370–374.
- (40) Wang, Y.; Huang, C.; Ma, X.; Zhao, J.; Guo, F.; Fang, X.; Zhu, Y.; Wei, Y. The optimum grain size for strength-ductility combination in metals. *Int. J. Plasticity* **2023**, *164*, No. 103574.
- (41) Wu, Y. C.; Shao, J. L. FCC-BCC phase transformation induced simultaneous enhancement of tensile strength and ductility at high strain rate in high-entropy alloy. *Int. J. Plasticity* **2023**, *169*, No. 103730.
- (42) Zhang, Z.; Huang, Q.; Zhou, H. High-entropy alloy nanocrystals with low-angle grain boundary for superb plastic deformability and recoverability. *Int. J. Plasticity* **2023**, *167*, No. 103679.
- (43) Segall, M. D.; Lindan, P. J.; Probert, M. A.; Pickard, C. J.; Hasnip, P. J.; Clark, S. J.; Payne, M. C. First-principles simulation: ideas, illustrations and the CASTEP code. *J. Phys.: Condens. Matter* **2002**, *14*, 2717.
- (44) Chen, X. Q.; Niu, H.; Li, D.; Li, Y. Modeling Hardness of Polycrystalline Materials and Bulk Metallic Glasses. *Intermetallics* **2011**, *19*, 1275–1281.
- (45) Tian, Y.; Xu, B.; Zhao, Z. Microscopic Theory of Hardness and Design of Novel Superhard Crystals. *Int. J. Refract. Met. Hard Mater.* **2012**, *33*, 93–106.
- (46) Zhao, Z.; Xu, B.; Tian, Y. Recent Advances in Superhard Materials. *Annu. Rev. Mater. Res.* **2016**, *46*, 383–406.
- (47) Hall, E. O. The deformation and ageing of mild steel. III. Discussion of results. *Proc. Phys. Soc. B* **1951**, *64*, 747.
- (48) Petch, N. J. The cleavage strength of polycrystals. *J. Iron Steel Inst.* **1953**, *174*, 25–28.
- (49) Tse, J. S.; Klug, D. D.; Gao, F. M. Hardness of nanocrystalline diamonds. *Phys. Rev. B* **2006**, *73*, No. 140102.
- (50) **Supplemental Material**.
- (51) Kresse, G.; Furthmüller, J. Efficient Iterative Schemes for ab initio Total-Energy Calculations Using a Plane-Wave Basis set. *Phys. Rev. B* **1996**, *54*, 11169.
- (52) Kresse, G.; Joubert, D. From Ultrasoft Pseudopotentials to the Projector Augmented-Wave Method. *Phys. Rev. B* **1999**, *59*, 1758.
- (53) Perdew, P.; Zunger, A. Correction to Density-Functional Approximations for Many-Electron Systems. *Phys. Rev. B* **1981**, *23*, 5048.
- (54) Monkhorst, H. J.; Pack, J. D. Special Points for Brillouin-Zone Integrations. *Phys. Rev. B* **1976**, *13*, 5188.
- (55) Togo, A.; Oba, F.; Tanaka, I. First-Principles Calculations of the Ferroelastic Transition Between Rutile-Type and $CaCl_2$ -Type SiO_2 at High Pressures. *Phys. Rev. B* **2008**, *78*, No. 134106.
- (56) Hill, R. The Elastic Behaviour of a Crystalline Aggregate. *Proc. Phys. Soc. London, Sect. A* **1952**, *65*, 349.
- (57) Drönskowski, R.; Blochl, P. E. Crystal orbital Hamilton populations (COHP): energy-resolved visualization of chemical bonding in solids based on density-functional calculations. *J. Chem. Phys.* **1993**, *97*, 8617–8624.
- (58) Maintz, S.; Deringer, V. L.; Tchougreff, A. L.; Drönskowski, R. LOBSTER: A tool to extract chemical bonding from plane-wave based DFT. *J. Comput. Chem.* **2016**, *37*, 1030–1035.
- (59) Roundy, D.; Krenn, C. R.; Cohen, M. L.; Morris, J. W., Jr Ideal Shear Strengths of fcc Aluminum and Copper. *Phys. Rev. Lett.* **1999**, *82*, 2713.
- (60) Zhang, Y.; Sun, H.; Chen, C. Superhard Cubic BC_2N Compared to Diamond. *Phys. Rev. Lett.* **2004**, *93*, No. 195504.
- (61) Liu, C.; Song, X.; Li, Q.; Ma, Y.; Chen, C. Smooth Flow in Diamond: Atomistic Ductility and Electronic Conductivity. *Phys. Rev. Lett.* **2019**, *123*, No. 195504.
- (62) Liang, H.; Li, H. F.; Li, Q.; Chen, C. Toughening a Superstrong Carbon Crystal: Sequential Bond-Breaking Mechanisms. *Phys. Rev. B* **2020**, *102*, No. 134105.
- (63) Liu, C.; Song, X.; Li, Q.; Ma, Y.; Chen, C. Superconductivity in Compression-Shear Deformed Diamond. *Phys. Rev. Lett.* **2020**, *124*, No. 147001.
- (64) Liu, C.; Song, X.; Li, Q.; Ma, Y.; Chen, C. Superconductivity in Shear Strained Semiconductors. *Chin. Phys. Lett.* **2021**, *38*, No. 086301.
- (65) Song, X.; Liu, C.; Li, Q.; Hemley, R. J.; Ma, Y.; Chen, C. Stress-induced high- T_c superconductivity in solid molecular hydrogen. *Proc. Natl. Acad. Sci. U. S. A.* **2022**, *119*, No. e212269111.

Supplemental Material on
Structural and Stress Response of Nanotwinned B₁₃CN Under Large Strains

Hui Liang^a, Di Wang^{a,b}, Xianqi Song^{a,b}, Qing Guo^{a*}, and Quan Li^{a,b*}

^a*State Key Lab of Superhard Materials and Key Laboratory of Material Simulation Methods & Software of Ministry of Education, College of Physics, Jilin University, Changchun 130012, China*

^b*International Center of Future Science, Jilin University, Changchun 130012, China*

*Corresponding author.

Email address: qingguo@jlu.edu.cn; liquan777@jlu.edu.cn.

Here we provide additional details supporting several results presented in the present work. Figure S1, Figure S2, S3, and Figure S4 correspond to Figure 4, Figure 5, and Figure 6 in the main text, respectively.

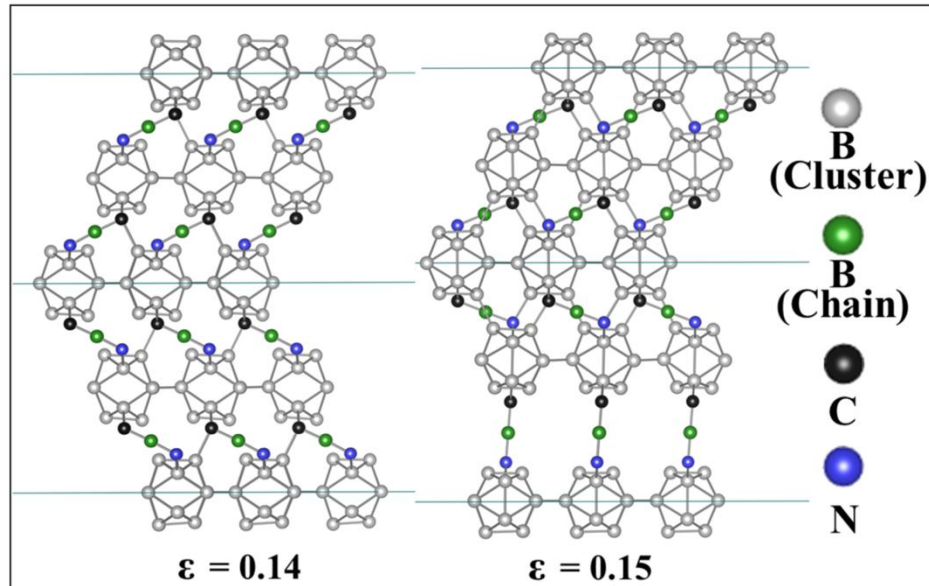


Figure S1. (Corresponds to Figure 4 in the main text.) Structural snapshots of nt-B₁₃CN deformed in the easy (i.e., with the lowest peak stress) [001] tensile direction at key strains.

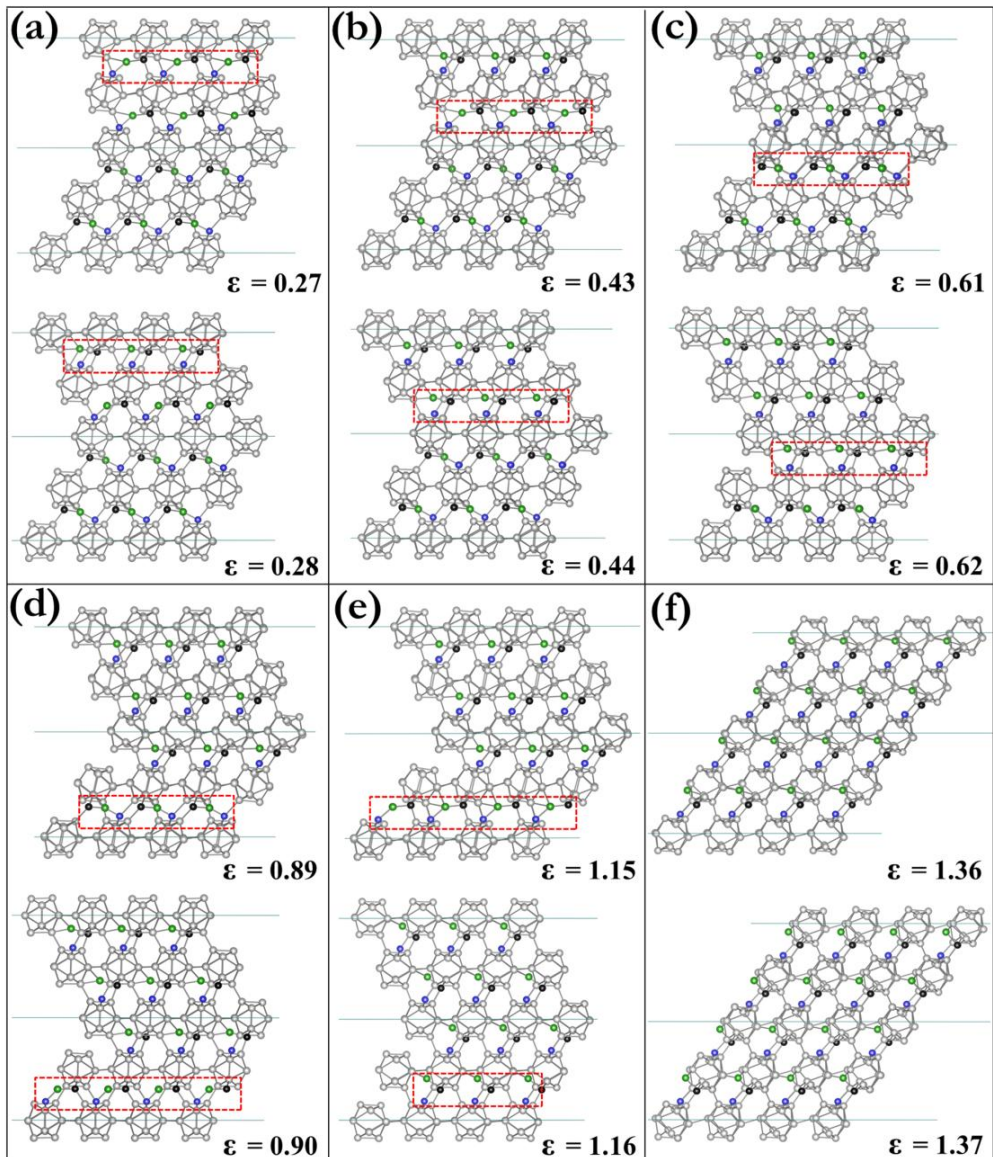


Figure S2. (Corresponds to Figure 5 in the main text.) (a-e) Structural snapshots of nt-B₁₃CN deformed in the easily (001)[100] shear slip direction at critical strains, corresponding to each peak stress (strain=0.27, 0.43, 0.61, 0.89, 1.15) point and stress release (strain=0.28, 0.44, 0.62, 0.90, 0.16) point. (f) Structural snapshots of stress peak (strain =1.36) and bond fracture (strain =1.37) points in sc-B₁₃CN degenerated from nt-B₁₃CN. Upper panel: peak stress, Lower panel: stress release.

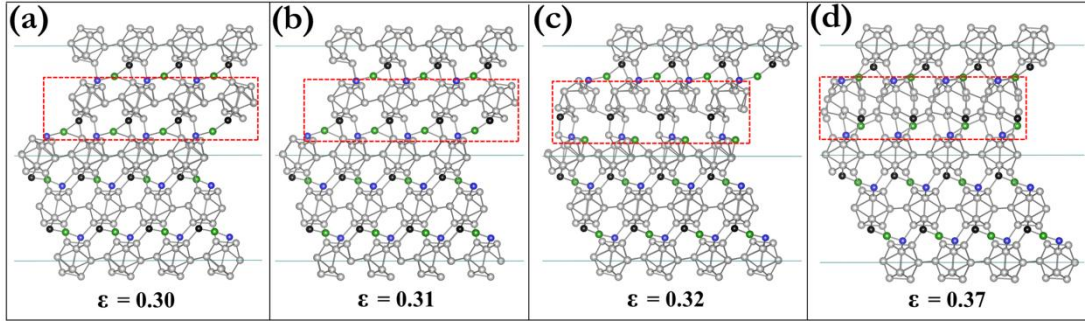


Figure S3. (Corresponds to Figure 5 in the main text.) (a-d) Structural snapshots of nt-B₁₃CN deformed in the easily (001)[110] shear slip direction at critical strains, corresponding to peak stress (strain=0.30) point and stress release (strain=0.31, 0.32, 0.37) point.

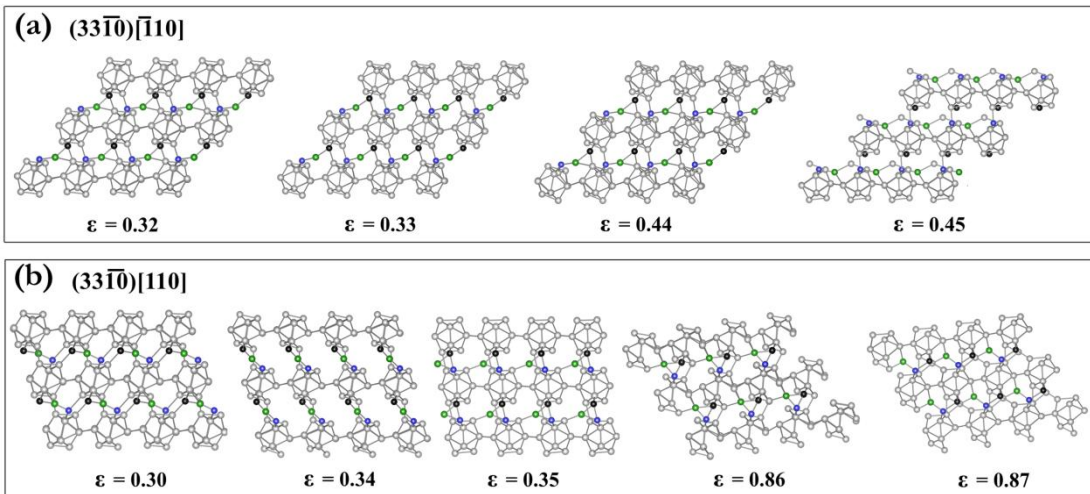


Figure S4. (Corresponds to Figure 6 in the main text.) Structural snapshots of sc-B₁₃CN under shear deformations in (a) (33̄10)̄[1̄100] direction, and (b) (33̄10)̄[100] direction.